Applied Surface Science 609 (2023) 155319

Contents lists available at ScienceDirect

Applied Surface Science

journal homepage: www.elsevier.com/locate/apsusc

Full Length Article

TEM study of the oxidation resistance and diffusion processes in a multilayered TiSiN/TiN(Ag) coating designed for tribological applications

Andrey Bondarev [a,*], Abbas Al-Rjoub [b,*], Talha Bin Yaqub [b,c], Tomas Polcar [a], Filipe Fernandes [b,c,d]

[a] Department of Control Engineering, Faculty of Electrical Engineering, Czech Technical University in Prague, Technicka 2, Prague 6, Czech Republic
[b] University of Coimbra, CEMMPRE - Centre for Mechanical Engineering Materials and Processes, Department of Mechanical Engineering, Rua Luís Reis Santos, 3030-788 Coimbra, Portugal
[c] IPN - LED&MAT - Instituto Pedro Nunes, Laboratório de Ensaios, Desgaste e Materiais, Rua Pedro Nunes, 3030-199 Coimbra, Portugal
[d] ISEP - School of Engineering, Polytechnic of Porto, Rua Dr. António Bernardino de Almeida 431, 4200-072 Porto, Portugal

ARTICLE INFO

Keywords:
Multilayered TiSiN/TiN(Ag) coating
TEM
Oxidation resistance
Diffusion
High-temperature behaviour

ABSTRACT

This work investigates the structure evolution of a multilayered TiSiN/TiN(Ag) coating with heating, oxide scale growth, diffusion processes occurring during oxidation, and changes in the structure and chemical composition of the non-oxidized zone. The coatings have a multilayered structure with a bilayer periodic thickness of ~40 nm. The TiN(Ag) layer consists of *fcc* TiN and Ag crystalline phases, where Ag nanocrystallites are homogenously distributed at the TiN grain boundaries. The TiSiN layer consists of *fcc* Ti—Si—N solid solution grains and an amorphous a-SiN_x phase which segregates at the Ti—Si—N grain boundaries. *In-situ* hot-XRD analysis shows that the first signs of oxidation occur at 800 °C, when rutile-TiO_2 starts to form. The oxidized part of the coating is Ag depleted, except the top layer terminating the structure, which contains some 1–3 nm Ag clusters. Ag diffuses towards the surface from oxidized zones. The cross-sectional analysis also shows no signs of recrystallization and structural changes, except for stress relaxation in the non-oxidized part after annealing at 800 °C. No Ag redistribution or diffusion is found in the non-oxidized part, even close to the interface with the oxide layer, which suggest effectiveness of the multilayered design to mitigate uncontrolled Ag migration towards the surface.

1. Introduction

Silver (Ag) is one of the most commonly used high-temperature solid lubricants among soft metals used to dope transition metal nitride, carbide, and carbonitride coatings. Ag is known to be chemically inert and immiscible in transition metal nitride and/or carbide coating systems [1–3]. Whilst the ceramic and carbide matrices ensure high hardness values, wear, oxidation resistance and thermal stability, Ag works as a solid lubricant phase due to its softness and low shear modulus. As reported in the literature, the addition of Ag in ceramic matrices enhances their overall tribological performance and lifetime [4–13]. Ag diffuses out to the surface of the film, establishing an Ag-rich tribolayer, which reduces friction and protects the coating from wear. Nevertheless, such improvements were shown to be short-lived due to the rapid release of the metal, its quick depletion from the entire volume of the coating, and the consequent loss of the low friction tribolayer after short operating periods. In general, Ag diffusion has also been shown to decrease the oxidation resistance of coatings, limiting their use at high temperatures. On the other hand, in TiAlSiN(Ag) [14] and TiNbCN(Ag) [15] coating systems, an improvement of the oxidation resistance of the coatings alloyed with Ag was found. This is due to the segregation of Ag metallic particles at the sites of coating cracks and oxidation, as well as chemical changes in the composition of the top oxide layer, which hinders inward O diffusion. Thus, as many studies point out, the challenge is to adequately control lubricant transport, with sufficient oxidation resistance, to allow both low friction and wear over long periods, in order to protect the surface of components utilized in different industrial fields. According to the literature, silver diffusion is influenced by the operating temperature, and the coating chemical composition, structure, and morphology [1,16–18].

Herein, the authors demonstrated that the TiSiN system, deposited either as a monolayer or in a multilayered configuration, offers the

* Corresponding authors.
E-mail addresses: bondaan2@fel.cvut.cz (A. Bondarev), abbas.al-rjoub@dem.uc.pt (A. Al-Rjoub).

https://doi.org/10.1016/j.apsusc.2022.155319
Received 20 June 2022; Received in revised form 10 October 2022; Accepted 13 October 2022
Available online 18 October 2022

possibility to tailor and control Ag diffusion from the entire volume of the coating. The amorphous SiN_x phase in the nanocomposite structure of the TiSiN layer acts as a barrier against diffusion [19–22], allowing Ag release to be tuned to a certain extent (depending on the chemical composition and architecture of the coating). The multilayered design of this coating system was shown to be more promising in controlling the Ag diffusion and oxidation resistance when compared to monolayer TiSiN(Ag). However, the oxidation resistance, diffusion processes occurring during annealing of multilayer TiSiN(Ag) coatings, and changes in the structure and chemical composition of the non-oxidized coating zone are not explored. Therefore, the understanding of those phenomena is of great importance in order to optimize the lubricious phase release, and in the design of coatings with long-term lubrication for high-temperature tribological applications.

This work presents a detailed investigation of the structure evolution of a multilayered TiSiN/TiN(Ag) coating concomitant with heating, oxide scale growth, diffusion processes occurring during oxidation, and changes in the structure and chemical composition of the non-oxidized zones.

2. Experimental

A multilayered TiSiN/TiN(Ag) coating was produced by DC reactive magnetron sputtering, using two high purity (99.9 %) Ti targets (100 × 200 mm) placed in a chamber with two cathodes facing each other. One of the targets has holes of 15 mm in diameter and 19 mm depth distributed uniformly in the target erosion zone; 8 of those holes were filled with Si pellets. This target was used to produce the TiSi adhesion layer, TiSiN gradient layer with increasing N concentration, and the TiSiN layers of the multilayer architecture. In the second target, 5 Ag pellets were placed in the holes to produce the TiN(Ag) layers of multilayer architecture. This number of pellets was selected to produce layers with approximately 14 at.% Ag. The multilayered architecture was ensured by the slow rotation of the substrate holder, rotating at the center of gravity of the chamber. The detailed description of the deposition parameters is presented in our previous work under the coating name of 'S1' [23], whilst a summary of the deposition parameters and the main properties of the coating are presented in Table 1.

The multilayered TiSiN/TiN(Ag) coating was isothermally oxidized in air at 800 °C for 2 h, in thermogravimetric analysis equipment. This temperature was selected based on the isothermal oxidation curves published in [23], where the first signs of oxidation is reported.

The cross-section lamellae from the as-deposited and oxidized coatings were prepared by focused ion beam (FIB) milling with Ga^+ ions using a dual-beam Helios NanoLab 660 microscope (FEI). Transmission electron microscopy (TEM) studies were carried out using a Tecnai F20 (FEI) microscope and a Titan Themis^3 (FEI) microscope equipped with a windowless Super-XG1 EDS detector (Thermo Fisher Scientific). Electron diffraction patterns were processed using CrysTBox software and the obtained d-spacings were used for the lattice parameter calculations [24]. The structure of the film was complemented by X-ray diffraction (XRD) analysis using Cu Kα1 radiation (λ = 1.54060 Å, 45 kV and 40 mA), acquired in grazing mode.

Table 1
Deposition parameters and properties of the coating.

Deposition parameters and selected properties of the coating	
Number of Ag rods (1.0 cm in diameter)	5
TiSi target power density (W/cm^2)	6.5
Ti (Ag) target power density (W/cm^2)	6.5
Substrate pulsed bias voltage (V)	−60
Working pressure (Pa)	0.34
Rotation speed for TiSi + TiSiN gradient layers (rotation/min) and deposition time	18 24 min
Rotation speed for TiN(Ag) + TiSiN multilayers (rotation/min) deposition time	0.9 1 h:20 min
Hardness (GPa)	26 ± 2
Young's modulus (GPa)	288 ± 13
Elastic strain to failure - H/E	0.09

The influence of the temperature evolution on the structure of the coating was evaluated using *in-situ* high temperature X-ray diffraction (XRD) in open air at temperature steps of RT, 600 °C, 750 °C, 800 °C, 850 °C, 900 °C, 950 °C, and RT after cooling down, using Co Kα radiation (1.789010 Å) equipment, acquired in conventional Bragg-Brentano mode. After performing each step, a holding time of 5 min was given for thermal stabilization, followed by an acquisition time of 45 min with a constant temperature ramp of 20 C/min.

The chemical states of the as-deposited and oxidized coatings were evaluated using X-ray Photoelectron Spectroscopy (XPS). The analysis was carried out with a monochromatic Al Kα X-ray source (1486.7 eV), operating at 15 kV (90 W), in FAT (Fixed Analyzer Transmission) mode, with a pass energy of 40 eV for the region ROI and 80 eV for the survey. The effect of the electric charge was corrected using the adventitious carbon peak (285.0 eV) as reference. The analyses were performed for the samples as received and after Ar^+ etching for 35 min. The peaks of the spectra were fitted using a Gaussian–Lorentzian peak shape and Shirley type of the background subtraction.

3. Results and discussion

3.1. Structure of the as-deposited coatings

Since this work is tightly connected with TEM results, before the main discussion of coating structures it is beneficial to highlight the TEM sample behaviour and evolution with time. The point that must be emphasised here is the long-term behaviour of the FIB lamellae fabricated for the investigations. The main TEM results presented were collected during the 24 h after FIB lift-out and polishing of each lamella. Fig. S1 in the supplementary information shows the evolution of the sample structure with time. It is obvious that silver diffusion and agglomeration into spherical particles take place over time. This happens due to the very small thickness of the lamella, and the appearance of a shortcut for Ag to diffuse toward the side walls of the lamella, and further surface diffusion and agglomeration [7]. The authors tried to minimize the time-affected changes in the samples and collected TEM results as fast as possible.

Bright field (BF) TEM and high-angle annular dark-field (HAADF) STEM images of the cross-section morphology of the as-deposited TiSiN/TiN(Ag) multilayered coating are shown in Fig. 1a. The total thickness of the coating including the TiSi and the gradient TiSiN adhesive layers is 2.6 μm. The multilayered coatings are designed with a periodic bilayer thickness of ~40 nm, as clearly displayed in the HAADF image in Fig. 1b. The EDS elemental maps of the multilayered coatings are shown in Fig. 1c, where it is possible to observe that the 20 nm thick brighter layer is TiN(Ag), whilst the 20 nm darker layer corresponds to TiSiN. The terminating (last) layer of the multilayered coating is the TiSiN layer as planed during the depositions. The thick dark layer on the top is the protective tungsten layer, deposited for FIB lamella preparation.

With the EDS analysis, it was possible to precisely acquire the average chemical composition of the individual layers in the multilayered architecture. The average concentration of the elements across the TiN(Ag) layer is the following: 34 at.% Ti, 51 at. % N, 14 at.% Ag, the TiSiN layer contains 31 at.% Ti, 15 at.% Si, and 54 at.% N. The analysis showed that both layers have an over-stoichiometric composition (i.e., Me/N < 1).

The XRD diffraction pattern of the as-deposited coating obtained in grazing incidence mode (GIXRD) is displayed in Fig. 2a. The diffraction peaks located at a 2θ of 36.7°, 42.6°, and 61.9° are assigned to the (111), (200), and (220) diffraction peaks of the *fcc* phase with lattice parameters very close to TiN (ICDD card no. 00-87-633), respectively. These peaks are raised from the cumulative signals of TiN-based fcc crystallites in the TiN-Ag, and TiSiN layers. Low intensity diffraction

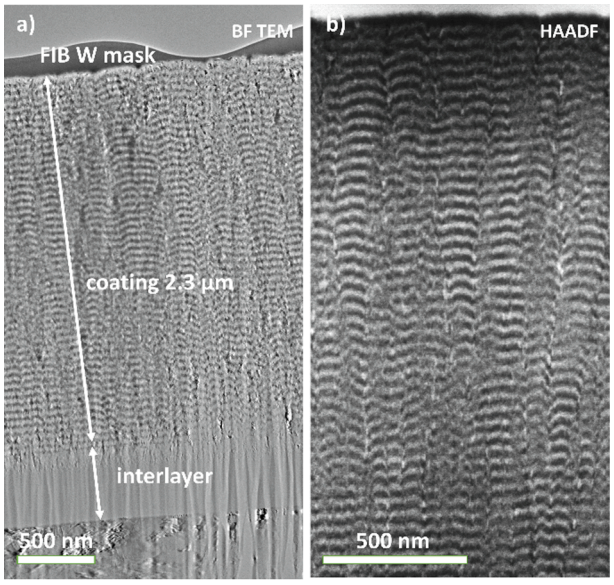

	Ti, at.%	Si, at.%	N, at.%	Ag, at.%
Ti-Si-N	31	15	54	0
TiN-Ag	34	<1	51	14

Fig. 1. TEM cross-section morphology in (a) BF TEM and (b) HAADF STEM imaging modes, as well as (c) elemental distribution in the as-deposited TiSiN/TiN(Ag) multilayered coating.

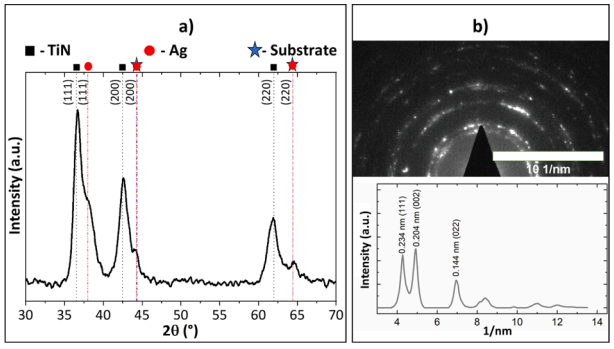

Fig. 2. (a) XRD diffraction patterns of the as-deposited coating deposited on Al_2O_3 substrate, obtained in grazing mode and (b) SAED pattern of the as-deposited coating.

peaks located at a 2θ of 38.1, 44.4, and 64.2° can be indexed as the Ag phase (ICDD card no. 00-001-1167).

The electron diffraction (SAED) pattern of the selected area acquired using a large aperture is presented in Fig. 2b. The bright diffraction rings in the SAED pattern correspond to the *fcc* structure. Since the lattice parameters of the crystalline phases presented in the multilayered coatings are very similar to each other, the observed pattern is a superposition of the signals from the fcc TiN, fcc Ag (TiN-Ag layer) and TiN-based fcc phase presented in TiSiN layers. HAADF STEM image and the EDS mapping of Ti and Ag signals, shown Fig. 3a and 3b respectively, confirming the presence of Ag. The light-grey areas in the HAADF image belong to silver-rich regions (all EDS maps are shown in Fig. S2 of the

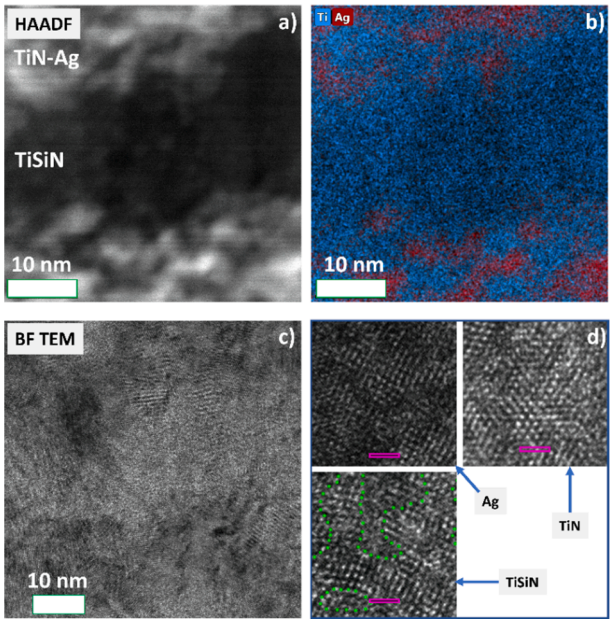

Fig. 3. (a) HAADF STEM image of the as-deposited TiSiN/TiN(Ag) coating structure, (b) EDS map showing the distribution of Ti and Ag, (c) BF TEM image of the as-deposited TiSiN/TiN(Ag) coating structure, and (d) HRTEM images (with 1 nm scale bar) of the different phases in the coating.

supplementary file). EDS mapping suggests that the light-grey areas in the HAADF image belong to silver-rich regions and that this phase exists in the structure as free nanocrystals that are not chemically bonded with other elements in the coating. Similar results were reported for different ceramic-silver coating systems containing Ag [8,15,25–27]. Finally, the azimuthally integrated SAED pattern exhibits peaks from the (1 1 1), (2 0 0), and (2 2 0) planes of the *fcc* lattice. The calculated lattice parameter of 0.417 nm does not characterize a particular phase but describes the as-deposited coating structure for further comparison with the annealed one.

Summarizing the data from HAADF STEM, EDS mapping, and BF TEM (Fig. 3c) it was possible to identify-three different crystalline phases in the coating: TiN grains and Ag in the TiN-Ag layer, crystalline TiN with Si in solid solution (Ti—Si—N), and an amorphous phase in the Ti—Si—N layer. The HRTEM insets in Fig. 3d show the fringe contrast of these identified crystal phases. It can be seen that the Ag nanocrystals ([0 0 1] zone axis) are characterized by a distorted crystalline structure, the TiN grain ([1 1 0] zone axis) in the TiN-Ag layer exhibits a crystalline structure with a lot of defects and some disordered/amorphous grain boundaries, and the Ti—Si—N grain consists of crystallites a few nm in size surrounded by amorphous phase (Fig. S2b).

Nano beam diffraction (NBD) with a spot size of around 5–6 nm allows us to obtain electron diffraction from individual nanolayers; lattice parameter values of 4.16 Å and 4.19 Å were found for the TiSiN and TiN (Ag) layers, respectively. The calculated values are in good agreement with the SAED results shown previously, in which the lattice parameter lies in the range of the average value between the lattice parameter of the two different layers. The lattice parameter values are lower than that of a typical TiN phase reported in the literature [28,29], which is 0.424–0.425 nm. Theoretical and experimental results show that an increase of Si concentration in $Ti_{1-x}Si_xN$ coatings leads to a decrease of *fcc* solid solution phase lattice parameters, as Si can substitute Ti atoms in the metallic sublattice [30,31]. On the other hand, Si can also form a SiN_x amorphous or crystalline phase between TiN grains [29,30,32,33].

In our coating, the TiSiN layer displays crystalline and amorphous zones, which taking into account the deposition temperature (<150 °C) and the Si concentration in this layer (~15 at.%), the presence of Si both in solid solution in the TiN lattice as well as the formation of SiN_x

amorphous phase is expected. The lower values of lattice parameters obtained by NBD when compared to values typical for TiN ($Ti_{1-x}Si_xN$) [30] can be attributed to the presence of intrinsic compressive stresses, which is quite common for magnetron sputtered TiSiN coatings [34,35]. On the other hand, in the TiSiN layer, the presence of Si in solid solution in the TiN lattice also contributes to the lattice parameter decrease due to the small atomic radius of Si compared to Ti. The TiN(Ag) layers reveal a slightly higher lattice parameter value. This fact can be associated with the presence of soft Ag clusters and grains located in TiN grain boundaries, which provide partial relaxation of the accumulated stresses [12] and a less distorted lattice due to the Si absence [30].

For further discussion of the oxidation and diffusion processes it is important to summarize the structure of the as-deposited TiSiN/TiN(Ag) multilayered coatings. The TiN(Ag) layers consist of fcc TiN crystallites, and free metallic Ag is located in TiN grain boundaries. The TiSiN layers consist of fcc Ti—Si—N solid solution crystallites surrounded by a-SiNx phase, which of the great importance for high-temperature performance of the coatings.

3.2. Evolution of coating structure with oxidation

The evolution of the microstructure during heating, which directly affects mechanical and tribological properties of the coatings, was tracked using TEM and *in situ* XRD diffraction analysis. Fig. 4 shows the obtained diffractograms; no extra peaks except the (111), (200), and (220) ones from the *fcc* phase are found in the as-deposited state. Indeed, there are no structural changes observed after annealing below a temperature of 800 °C. The peaks associated with the Ag are also detected in the XRD diffractograms, and strictly increased with increasing annealing temperature, suggesting the agglomeration of Ag on the top surface of the coating, as will be seen later (Fig. 5b). The first signs of oxidation are observed at 800 °C, where several low intensity peaks related to the rutile TiO_2 phase (ICDD card no. 76-0649) are reported. With a further temperature raise, the intensity of the rutile peaks increases, whilst diffraction peaks assigned to the *fcc TiN* phase lose their intensity. The oxidation of the *fcc* matrix phase is fully accomplished at 950 °C, where only the rutile TiO_2 phase can be detected by XRD. It is also worth mentioning that diffraction peaks of Ag and TiO_2 at high temperature are shifted to lower diffraction angles due to the thermal expansion of the lattice. However, the peaks are shifted back to the original positions after cooling down from 950 to 25 °C.

Furthermore, surface SEM analysis of the as-deposited and annealed coating (at 800 °C for 2 h, the temperature which promoted the first structure changes) is shown in Fig. 5. The as-deposited coating reveals a fairly smooth surface with insignificant defects, whilst the annealed

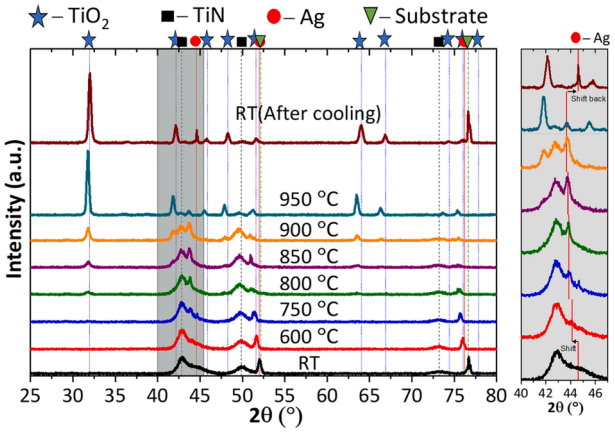

Fig. 4. *In situ* XRD spectra of the oxidized coating deposited on FeCrAlY alloy at different temperatures, including a magnified picture of the range of 2θ 40–46°, showing the shift and the increase of Ag peak with increasing annealing temperature.

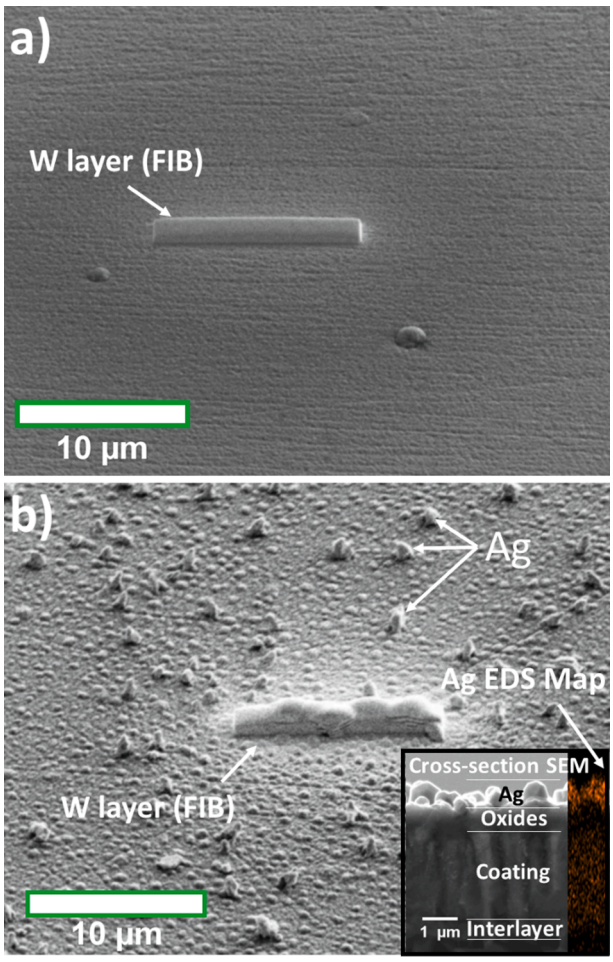

Fig. 5. Surface morphology of the: (a) as-deposited and (b) oxidized coating, showing the Ag out diffusion. The inset in (b) is a SEM cross-section of the oxidized coating with Ag EDS map.

coating displays a rough morphology with spherical features grown on top. EDS analysis conducted on the features revealed that they correspond to Ag particles. This corroborates the SEM picture shown in Fig. 5b, where the growth of the spherical particles on the top-most part of the oxide scale are seen clearly.

In order to gain further insight into the microstructure, phase and elemental composition of the cross-section of the oxidized coating, TEM investigations were conducted. The HAADF STEM cross-section image of the oxidized coating and its corresponding EDS elemental distribution maps are shown in Fig. 6. An oxidized layer of ~330 nm thick is formed on the top (Fig. 6a), meaning that at a temperature of 800 °C only a small part (~15 % of total thickness) of the coating is oxidized. Fig. 6b overviews the interface between oxidized and unoxidized coating and two distinctive regions are observed: 1) regions with sharp interface (mainly) (Fig. 6c), 2) transition regions where oxidation has been started, labelled as O-attacked (Fig. 6d).

The fully oxidized layer above the interface is composed of Ti, O and Si, while the N is confirming the surface oxidation and release of N from the structure (Fig. 6b). The average composition of the oxide scale is summarized in the table inserted in Fig. 6b, it can be seen the Ti/O ratio is close to TiO2 phase. The EDS elemental maps also revealed that the multilayered architecture of the coating is preserved, as it is possible to distinguish two types of oxide layer resulting from the oxidation of the TiSiN and TiN(Ag) layers, respectively. The expansion of the individual oxidized layers is attributed to a larger volume of oxide phases compared to pristine nitride phases.

The Ag particles were partially removed from the top surface of the

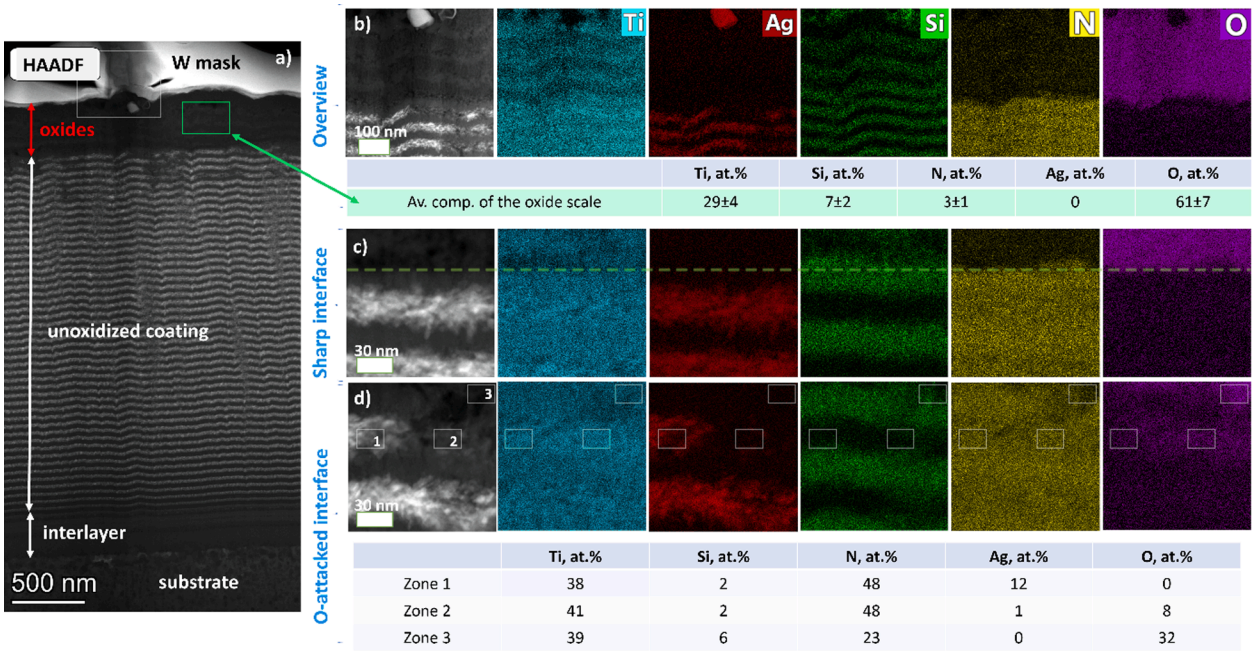

Fig. 6. Cross-sectional HAADF images and corresponding elemental maps of the oxidized TiSiN/TiN(Ag) multilayered coating. (a) Low-mag image, (b) overview of the oxide scale, (c) sharp interface between oxide scale and unoxidized coating, (d) O-attacked interface.

oxidized coating by Ga ions during FIB polishing, but they are still clearly presented in the cross-section view as shown by the EDS Ag map in Fig. 6b. The oxidized zone of the coating is Ag depleted. According to the EDS maps, it can be seen that silver from the oxidized zone diffuses out to the top surface of the oxide scale and forms agglomerates. Some Ag also diffuses out from the top adjacent non-oxidized layers. The silver diffusion to the top surface of the oxide layer was observed for other Ag-doped ceramic coatings during oxidation. Meanwhile, there is no general rule how Ag diffusion affects the oxidation resistance of the ceramic coatings, and it appears as tradeoff between two mechanisms. Ag diffusion to the surface i) creates extra paths for ions diffusion and, consequently, increases the oxidation rate and the thickness of the oxide scale [23,36] or ii) causes Ag to segregate at coating defect sites, slowing down the inward diffusion of oxygen atoms, and increasing oxidation resistance [14,15].

The chemical composition of the non-oxidized TiSN and TiN(Ag) layers underneath the oxide layer and adjacent to the interface region of the oxides layer remains the same as the as-deposited coating (Fig. 6c under the dashed line showing the interface). This implies that TiSiN layers hinder the fast Ag outward diffusion towards the non-oxidized zone. Meanwhile, some zones of O-attacked interface were captured as well (Fig. 6d). From the EDS analysis of a TiN(Ag) layer adjacent to the oxidized/non-oxidized coating interface, the first step of the oxygen diffusion can be tracked. The TiN(Ag) layer adjacent to the interface (Fig. 6d) reveals two characteristic areas: one with Ag and another without Ag. According to EDS analysis taken from the boxed areas (zones 1, 2, 3 in the table on Fig. 6d), diffusion of O (~8 at.%) in the TiN (Ag) layer is enough to trigger the outward Ag diffusion, and its concentration becomes zero in the O-containing part of the layer, while O-free parts still possess around 8 at.% of Ag (almost the same as the as-deposited state). Thus, it can be assumed that Ag release is not only temperature activated. Another important factor that promotes Ag diffusion from the nitride matrix towards the oxide scale is the differences in Ag wettability of nitride and oxide phases. Formation of the TiN (Ag)/oxide interface accelerates the Ag diffusion due to the fact that Ag does not wet TiN. The Ag wettability of TiO2 is noticeably lower (lower contact angle), indicating a hydrophilic state [37,38]. These differences in contact angles may explain a phenomenon whereby Ag covers preferentially oxidation sites on the surface of partially oxidized TiN-based coatings instead of non-oxidized parts [15].

Finally, by analyzing the topmost zone of the oxidized coating (Fig. 7), it can be assumed that the nanoscale segregation takes place on the sample surface. Indeed, areas enriched in Ti and depleted in Si are found on the top surface, suggesting the formation of separated TiO_2-based and SiO_2-based oxides, as observed in monolithic TiSiN coatings [28,39,40]. At the same time oxygen is distributed homogeneously across the oxide scale (Fig. S3). G. Greczynski et al. reported this phenomenon for single layer $Ti_{1-x}Si_xN$ coatings with $0.13 \leq x \leq 0.31$, where Si-rich coatings exhibit a formation of the glassy layer, which consists of complex Me—Si—O [39–42]. In the present study we assume the well pronounced segregation of TiO_2-based and SiO_2-based oxides takes place at top surface of the oxide layer, as shown in the Fig. 7 (magnified map of the boxed area in Fig. 6a).

Another important point that has to be raised is the location of the Ag agglomerate on the top surface of the coating after oxidation. Elemental mapping shows that the Ag agglomerate sits on the TiO_2-based surface. This effect was observed for the Ag-doped ceramic during oxidation, where silver segregates at the sites of coating defects or oxidation, slowing down the inward diffusion of oxygen atoms, and increasing oxidation resistance [14,15].

Fig. 8a presents the BF TEM contrast of the oxide scale with a mark where the diffraction pattern was acquired. SAED taken from the oxide layer of the top of the annealed multilayered TiSiN/TiN(Ag) coatings

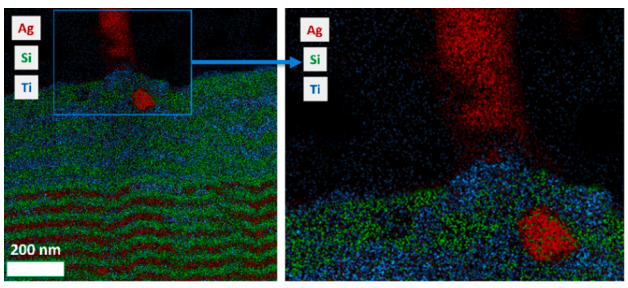

Fig. 7. EDS elemental maps of the top part of the oxide scale after oxidation annealing. Presented area is marked by grey box in Fig. 6a.

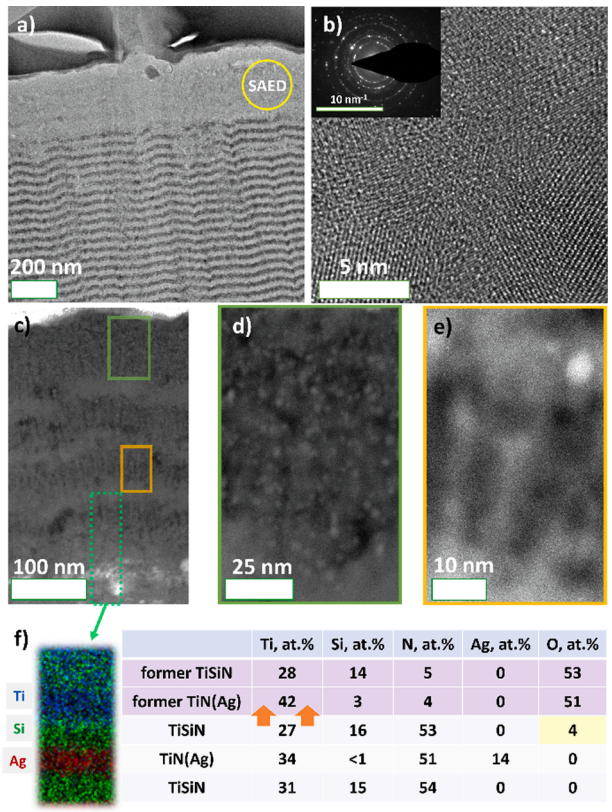

	Ti, at.%	Si, at.%	N, at.%	Ag, at.%	O, at.%
former TiSiN	28	14	5	0	53
former TiN(Ag)	42	3	4	0	51
TiSiN	27	16	53	0	4
TiN(Ag)	34	<1	51	14	0
TiSiN	31	15	54	0	0

Fig. 8. (a) Cross-sectional BF TEM image of the coatings after oxidation annealing, (b) HRTEM image of the oxide scale, (c) HAADF overview of the oxide scale, (d) HAADF image of the former Ti—Si—N layer that terminates the multi-layered structure, and (e) HAADF image oxidized Ti—Si—N layer in the middle of the oxide scale.

(Fig. 8b inset) shows a ring pattern. All signals belong to the polycrystalline rutile TiO_2 phase. Rutile (1 1 0), (0 1 1), (1 1 1), (1 2 1), and (0 0 2) reflections are identified in the SAED pattern; no other crystalline compounds are observed in the oxide layer. However, according to the EDS maps shown in Figs. 6 and 7, regions enriched simultaneously with Si and O are also presented. This phase is well known to be amorphous and therefore its presence does not significantly contribute to electron diffraction pattern. The presence of amorphous regions is clearly visible in the HRTEM image of the oxide layer (Fig. 8b), supporting this theory. The presence of amorphous complex Ti—Si—O oxide should not be discarded, as in some zones of the elemental maps of Fig. 7, overlapping of the Ti, Si, O signals is perceived. G. Greczynski et al. detected this disordered phase after oxidation of monolithic TiSiN coatings.

Fig. 8c shows HAADF image of the entire cross-section of the oxide scale with 3 boxed areas of interests: terminating TiSiN layer after oxidation (green box), TiSiN layer after oxidation in the middle part of the scale (orange box) and oxidized/non-oxidized interface (turquoise dashed box). The HAADF image (Fig. 8d) coupled with EDS maps (Fig. S4a) of the terminating oxidized TiSiN layer clearly show that some segregations into TiO_2-based and SiO_x-based oxides have also taken place within former Ti—Si—N layers. The topmost layer reveals a composite structure with two types of regions both < 10 nm in size: i) one enriched by Ti and ii) another enriched by Si. This layer also contains spherical Ag particles, 1–3 nm in diameter, scattered across the entire terminating top layer. Nevertheless, concentration of silver is very low, local EDS analysis of the area with nanoparticles shows only 1 at.% of Ag (Fig. S4a). One can notice that the terminating top layer is thicker compared to other oxidized layers. Probably this is attributed to the fact that initial oxidation starts at solid/gas interface and TiO2 growth and expansion are not restricted. In this way, some porosity in terminating layer cannot be excluded consequently creating a place for Ag, that is why 1–3 nm Ag particles are scattered only in this top layer after oxidation.

In the TiSiN layer after oxidation in the middle part of the scale Ag particles are almost absent, which confirms the diffusion of Ag towards the surface (Fig. 8e). Also, the segregation of TiO_2-based and SiO_x-based oxides is more pronounced along the vertical direction (main diffusion route), as reported by Y. Moritz et al. for oxidized TiSiN coatings [28]. The EDS mapping of this area indicates an obvious segregation (see Fig. S4b in supplementary file). In this case the segregation occurs in former Ti—Si—N layers in the nano-laminated structure, as was detected for bulk TiSiN coatings [19,28]. We assume that the processes in individual Ti—Si—N layers can proceed in a similar way to a bulk ceramic in the Ti—Si—N system, where oxidation starts from fcc Ti—(Si)—N crystallites that are oxidized to TiO_2. The titanium deficiency in the crystallites close to the coating's surface (due to outward diffusion of Ti) causes an increase in the nitrogen dissociation partial pressure, which is released in a gaseous form. Pores, formed because of coalescence of the vacancies induced by the motion of Ti and N, can appear in the sites of former Ti—(Si)—N crystallites [43]. Then, a-SiNx phase is oxidized by the vacancy oxidation or by displacement reaction with the formation silicon oxynitride at the first stage and with formation of SiOx in the later stage of oxidation process [44,45]. We suppose, that the TiSiN/TiN (Ag) multilayered coatings demonstrate similar diffusion/oxidation mechanisms. In the as-deposited state, homogeneous distribution of Ti is observed, while after oxidation the Ti signal becomes more intensive in former TiN(Ag) layers (Fig. 6b and Fig. 8f). Once O reaches the TiN(Ag) layer (which has lower oxidation resistance and can be transformed into TiO_2 faster than in the Ti—Si—N layer), the driving force for Ti diffusion from non-oxidized regions appears. EDS analysis of the oxidized/non-oxidized interface shows decrease in Ti concentration in the TiSiN layer adjacent to oxide scale (Fig. 8f). Titanium diffusion is faster than oxygen diffusion through the newly formed rutile crystals [19,46]. In the same way, the re-distribution mechanism of Ti and Si can happen on the nanoscale in Ti—Si—N layers (Fig. S3) [43,47].

The EDS profiling under the oxide part of the coating, showing the distribution of the elements through the coating thickness, is presented in Fig. 9a and b. The chemical composition of the non-oxidized TiSiN and TiN(Ag) layers underneath the oxide layer and adjacent to the interface region of the oxides layer remains stable. Additionally, the multilayered design of the TiSiN/TiN(Ag) coatings prevents the Ag "sweating" that often occurs even immediately after deposition of the coatings [48–50]. It is noteworthy that no nanoscale segregation or recrystallization in individual non-oxidized TiN(Ag) layers is detected, even in the very top of the non-oxidized part of the coating (Fig. 9 c and d).

The structural changes occurring in the non-oxidized part of the coatings were investigated by electron diffraction (SAED, NBD). Processing of NBD patterns from individual nanolayers after annealing gives lattice parameter values of 0.423 nm and 0.422 nm for the TiSiN and TiN (Ag) layers, respectively, as shown in Fig. 10. The increase of the lattice parameters for the annealed coating compared with the as-deposited one from 0.416 to 0.423 nm and 0.419 to 0.423 nm may be attributed to a relaxation of stresses in the coating. The SAED technique, which averages lattice parameters from individual layers, also indicates relaxation of compressive stresses after annealing. It is important to notice that the TiSiN layers show more dramatic changes in lattice parameter values with annealing, which points out that this layer was under a higher level of stresses as compared to the TiN(Ag) one.

To support the TEM results, which give no precise information about the chemical bonds between elements, XPS analysis was conducted. The XPS core-level spectra of Ti 2p, Si 2p, N 1s, Ag 3d, and O 1s of the as-deposited coating are shown in Fig. 11. For the Ti 2p core level spectrum (taken from the as-deposited surface) a contribution of three components is found. The peaks centered at 458.8 eV, 456.9 eV and 455.1 eV are assigned to Ti—O (IV), Ti—O (lower oxidation state)

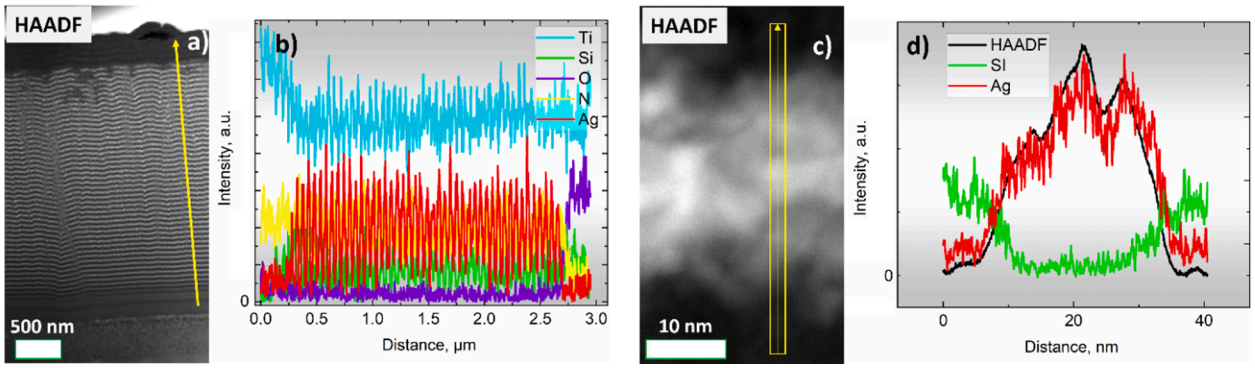

Fig. 9. (a, c) HAADF images and (b, d) corresponding EDS elemental distribution profiles showing an absence of redistribution of the elements after annealing.

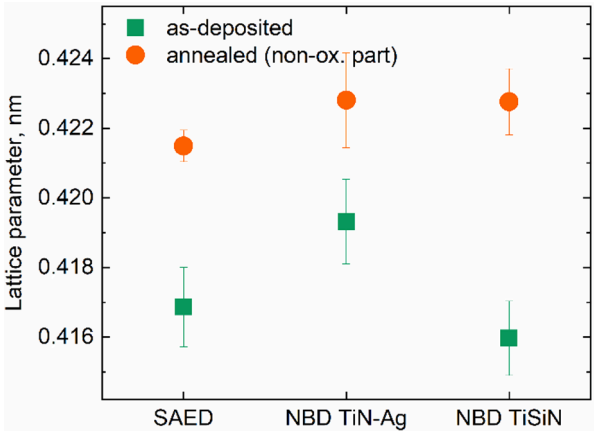

Fig. 10. The *fcc* lattice parameters obtained using SAED (average from the large area) and NBD (from individual layer) techniques.

denoted as TiO_x, and Ti—(Si)—N, respectively [51,52]. Here it is important to note that the exact environment of Ti atoms in the Ti—Si—N system is hard to interpret, since binding energies for Ti—N and Ti—Si—N solid solution are rather similar [53,54]. The presence of oxide components is due to oxygen absorption and oxidation after sample storage under ambient atmosphere. Eventually, after the Ar^+ etching, the Ti—Si—N component dominates the spectrum. The Ti 2p core level spectrum after oxidation shows peaks ascribed to Ti—O (IV), and the spectrum reveals a shoulder from lower Ti oxides or a mixed Ti—O—Si oxide after etching [55]. This difference in environment of Ti atoms on the surface and after etching matches the above-mentioned TEM data, where segregation of TiO_2-based and SiO_x-based oxides is more pronounced on the surface of the oxide scale. The Si 2p core level spectra exhibit a contribution of Ti—Si—N and Si-N components, which confirm the co-existence of Si in Ti—Si—N solid solution and in amorphous SiN_x matrices. Oxidation leads to the formation of Si-O bonds, and the Ti—Si—N and Si-N peaks disappear as expected. The N 1s spectra, before and after etching of the as-deposited coating, reveal peaks centered at 397.2 eV due to N in Ti—Si—N [39,53], with the small contribution from a peak assigned to the N—Si at 398.0 eV also present [56–58]. After the annealing, N is absent in the oxide scale, what was actually seen by EDS. The Ag 3d spectrum shows a low intensity signal in the as-deposited state, while oxidation triggers Ag diffusion towards the surface and the intensity increases significantly. The Ag 3d spectrum of the oxidized coating can be deconvoluted into two components centered at 368.3 and 368.5 eV, with different FWHM values, which corresponds to values typical of Ag—Ag bulk metallic bonds and Ag-Ag bonds from clusters, respectively [59–62]. This suggests that Ag can be presented in the coating as metallic grains and clusters, which agrees with the TEM data discussed earlier. The most interesting feature of the O 1s spectrum is found after oxidation, when an obvious separation of the O—Si and O—Ti peaks occurred. This confirms a segregation of TiO_2-based and SiO_x-based oxides. After the etching of the oxidized coating, the O 1s spectrum is similar to that of the as-deposited coating.

4. Conclusions

In this work, the structure evolution caused by high-temperature oxidation, oxide scale growth, diffusion processes and changes in the structure and chemical composition of the non-oxidized zone of a multilayered TiSiN/TiN(Ag) coating designed for high temperature applications are investigated.

The following conclusions can be drawn:

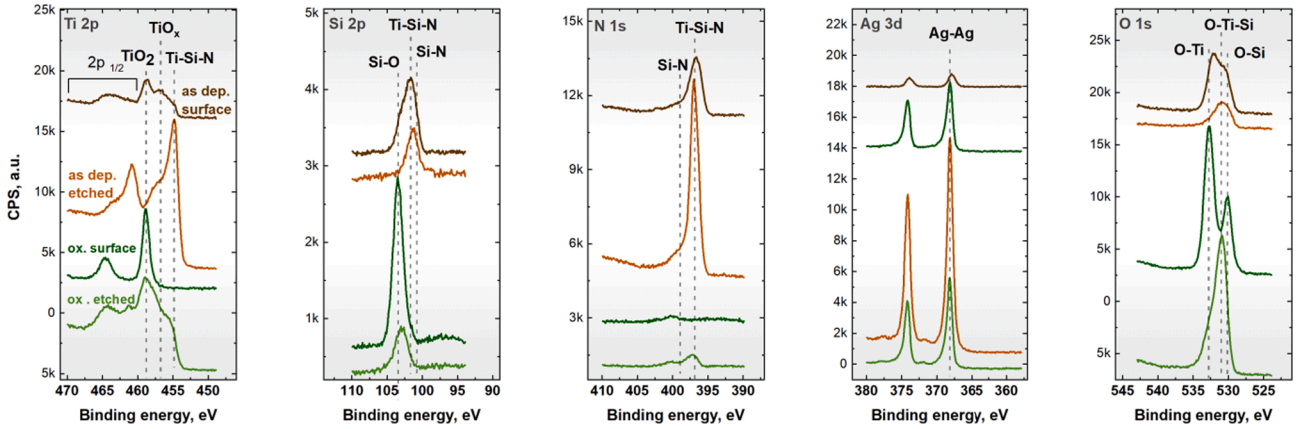

Fig. 11. X-ray photoelectron spectroscopy of the as-deposited and annealed coatings before and after Ar^+ etching.

1) The multilayered design of the coating can hinder the undesirable diffusion of Ag from the volume of the coating towards the surface with heating.
2) Oxidation of the multilayered TiSiN/TiN(Ag) coating starts at 800 °C with the formation of crystalline rutile TiO_2 and amorphous SiO_x-based oxide. These phases tended to be segregated.
3) No signs of recrystallization of pristine *fcc* TiN + *fcc* Ag phases in TiN(Ag) layers and *fcc* Ti—Si—N solid solution and a-SiN_x phases in TiSiN layers is detected in the non-oxidized part of the coatings after 2 h annealing at 800 °C.
4) In the multilayered TiSiN/TiN(Ag) coating the oxidation kinetics are controlled by inward diffusion of O and outward diffusion of Ti. Ag diffusion towards the surface is temperature activated and driven by wetting of oxide phases.
5) Diffusion of Ag from the oxide scale to the surface tends to agglomerate on the TiO_2-based sites.

CRediT authorship contribution statement

Andrey Bondarev: Conceptualization, Validation, Investigation, Visualization, Writing - review & editing. **Abbas Al-Rjoub:** Conceptualization, Investigation, Validation, Methodology, Writing - original draft. **Talha Bin Yaqub:** Investigation. **Tomas Polcar:** Funding acquisition. **Filipe Fernandes:** Conceptualization, Validation, Project administration, Funding acquisition, Writing - review & editing.

Declaration of Competing Interest

The authors declare that they have no known competing financial interests or personal relationships that could have appeared to influence the work reported in this paper.

Data availability

The data that support the findings of this study are available from the corresponding author upon reasonable request.

Acknowledgements

This research is sponsored by national funds through FCT – Fundação para a Ciência e a Tecnologia, under the projects: UIDB/00285/2020, SMARTLUB—ref. "POCI-01-0145-FEDER-031807". MCTool21 project "Manufacturing of cutting tools for the 21st century: from nano-scale material design to numerical process simulation" (reference: POCI-01-0247-FEDER-045940), co-financed by the European Regional Development Fund, through Portugal 2020 (PT2020), and by the Competitiveness and Internationalization Operational Programme (COMPETE 2020). A.B. acknowledges the support of the project "International Mobility of the scientific workers MSCA-IF IV at Czech Technical University in Prague, Grant No: CZ.02.2.69/0.0/0.0/20_079/0017983 and CzechNanoLab Research Infrastructure supported by MEYS CR (LM2018110). T.P. acknowledges support from the project CAAS CZ.02.1.01/0.0/0.0/16-019/0000778.

Appendix A. Supplementary data

Supplementary data to this article can be found online at https://doi.org/10.1016/j.apsusc.2022.155319.

References

[1] F.C. Thompson, F.M. Kustas, K.E. Coulter, G.A. Crawford, Influence of chemical vapor precursor flow rate on the structure and thermal stability of phase-modulated VSiCN/Ag coatings, J. Vac. Sci. Technol., A 39 (6) (2021) 063409, https://doi.org/10.1116/6.0001302.
[2] J.F. Pierson, D. Wiederkehr, A. Billard, Reactive magnetron sputtering of copper, silver, and gold, Thin Solid Films 478 (2005) 196–205, https://doi.org/10.1016/j.tsf.2004.10.043.
[3] J.E. Krzanowski, Phase formation and phase separation in multiphase thin film hard coatings, Surf. Coat. Technol. 188–189 (2004) 376–383, https://doi.org/10.1016/j.surfcoat.2004.08.028.
[4] P. Basnyat, B. Luster, Z. Kertzman, S. Stadler, P. Kohli, S. Aouadi, J. Xu, S. R. Mishra, O.L. Eryilmaz, A. Erdemir, Mechanical and tribological properties of CrAlN-Ag self-lubricating films, Surf. Coat. Technol. 202 (2007) 1011–1016, https://doi.org/10.1016/j.surfcoat.2007.05.088.
[5] W. Gulbiński, T. Suszko, Thin films of Mo2N/Ag nanocomposite-the structure, mechanical and tribological properties, Surf. Coat. Technol. 201 (2006) 1469–1476, https://doi.org/10.1016/j.surfcoat.2006.02.017.
[6] F. Fernandes, A. Al-Rjoub, D. Cavaleiro, T. Polcar, A. Cavaleiro, Room and high temperature tribological performance of multilayered tisin/tin and tisin/tin(Ag) coatings deposited by sputtering, Coatings 10 (2020) 1–13, https://doi.org/10.3390/coatings10121191.
[7] V. Lenzi, A. Cavaleiro, F. Fernandes, L. Marques, Diffusion of silver in titanium nitride: insights from density functional theory and molecular dynamics, Appl. Surf. Sci. 556 (2021) 149738, https://doi.org/10.1016/j.apsusc.2021.149738.
[8] H. Ju, L. Yu, D. Yu, I. Asempah, J. Xu, Microstructure, mechanical and trobological properties of TiN-Ag films deposited by reactive magnetron sputtering, Vacuum 141 (2017) 82–88, https://doi.org/10.1016/j.vacuum.2017.03.026.
[9] D.V. Shtansky, A.V. Bondarev, P.V. Kiryukhantsev-Korneev, T.C. Rojas, V. Godinho, A. Fernández, Structure and tribological properties of MoCN-Ag coatings in the temperature range of 25–700 °c, Appl. Surf. Sci. 273 (2013) 408–414, https://doi.org/10.1016/j.apsusc.2013.02.055.
[10] M. John, P.L. Menezes, Self-lubricating materials for extreme condition applications, Materials. 14 (19) (2021) 5588, https://doi.org/10.3390/ma14195588.
[11] A.V. Bondarev, P.V. Kiryukhantsev-Korneev, D.A. Sidorenko, D.V. Shtansky, A new insight into hard low friction MoCN-Ag coatings intended for applications in wide temperature range, Mater. Des. 93 (2016) 63–72, https://doi.org/10.1016/j.matdes.2015.12.131.
[12] A.V. Bondarev, M. Golizadeh, N.V. Shvyndina, I.V. Shchetinin, D.V. Shtansky, Microstructure, mechanical, and tribological properties of Ag-free and Ag-doped VCN coatings, Surf. Coat. Technol. 331 (2017) 77–84, https://doi.org/10.1016/j.surfcoat.2017.10.036.
[13] A.V. Bondarev, D.G. Kvashnin, I.V. Shchetinin, D.V. Shtansky, Temperature-dependent structural transformation and friction behavior of nanocomposite VCN-(Ag) coatings, Mater. Des. 160 (2018) 964–973, https://doi.org/10.1016/j.matdes.2018.10.029.
[14] A. Al-Rjoub, A. Cavaleiro, T.B. Yaqub, M. Evaristo, N.M. Figueiredo, F. Fernandes, TiAlSiN(Ag) coatings for high temperature applications: the influence of Ag alloying on the morphology, structure, thermal stability and oxidation resistance, Surf. Coat. Technol. 442 (2022) 128087, https://doi.org/10.1016/j.surfcoat.2022.128087.
[15] A.V. Bondarev, P.V. Kiryukhantsev-Korneev, E.A. Levashov, D.V. Shtansky, Tribological behavior and self-healing functionality of TiNbCN-Ag coatings in wide temperature range, Appl. Surf. Sci. 396 (2017) 110–120, https://doi.org/10.1016/j.apsusc.2016.10.188.
[16] C. Hong, Y. Huan, P. Zhang, K. Zhang, P. Dai, Effect of silver content on the microstructure, thermal stability and mechanical properties of CrNx/Ag nanocomposite films, Ceram. Int. 47 (2021) 25324–25336, https://doi.org/10.1016/j.ceramint.2021.05.254.
[17] P. Bilek, P. Jurci, M. Novak, M. Hudakova, L. Caplovic, Tribological and mechanical properties of Cr2N–11Ag-coatings deposited on Cr–V ledeburitic steel, Wear 340–341 (2015) 47–52, https://doi.org/10.1016/j.wear.2015.03.019.
[18] H. Guo, M. Han, W. Chen, C. Lu, B. Li, W. Wang, J. Jia, Microstructure and properties of VN/Ag composite films with various silver content, Vacuum 137 (2017) 97–103, https://doi.org/10.1016/j.vacuum.2016.12.020.
[19] M. Diserens, J. Patscheider, F. Le, Mechanical properties and oxidation resistance of nanocomposite TiN – SiNx physical-vapor-deposited thin films, Surf. Coat. Technol. 121 (1999) 158–165, https://doi.org/10.1016/S0257-8972(99)00481-8.
[20] P. Steyer, D. Pilloud, J.F. Pierson, J.P. Millet, M. Charnay, B. Stauder, P. Jacquot, Oxidation resistance improvement of arc-evaporated TiN hard coatings by silicon addition, Surf. Coat. Technol. 201 (2006) 4158–4162, https://doi.org/10.1016/j.surfcoat.2006.08.023.
[21] S. Vepřek, S. Reiprich, L.i. Shizhi, Superhard nanocrystalline composite materials: the TiN/Si3N4 system, Appl. Phys. Lett. 66 (20) (1995) 2640–2642, https://doi.org/10.1063/1.113110.
[22] G. Bilger, T. Voss, T. Schlenker, A. Strohm, High-temperature diffusion barriers from Si-rich silicon-nitride, Surface and Interface, Analysis 38 (2006) 1687–1691, https://doi.org/10.1002/sia.2396.
[23] A. Al-Rjoub, A. Cavaleiro, S.S. Rajput, F. Fernandes, High Si multilayered TiSiN/TiN(Ag) films with superior oxidation resistance, J. Mater. Res. Technol. 12 (2021) 2340–2347, https://doi.org/10.1016/j.jmrt.2021.04.040.
[24] M. Klinger, More features, more tools, more CrysTBox, J. Appl. Crystallogr. 50 (2017) 1226–1234, https://doi.org/10.1107/S1600576717006793.
[25] F. Yan, B. Jiang, Z. Wang, J. Shi, C. Yang, D. Dong, X. Wang, Thermal stabilization of nanocrystalline promoting conductive corrosion resistance of TiN–Ag films for metal bipolar plates, Vacuum 195 (2022), 110631, https://doi.org/10.1016/j.vacuum.2021.110631.
[26] D. Yu, L. Yu, I. Asempah, H. Ju, J. Xu, S. Koyama, Y. Gao, Microstructure, mechanical and tribological properties of VCN-Ag composite films by reactive

magnetron sputtering, Surf. Coat. Technol. 399 (2020), 126167, https://doi.org/10.1016/j.surfcoat.2020.126167.
[27] K. Kitawaki, K. Kaneko, K. Inoke, J.C. Hernandez-Garrido, P.A. Midgley, H. Okuyama, M. Uda, Y. Sakka, Fabrication and characterization of TiN-Ag nanodice, Micron. 40 (2009) 308–312, https://doi.org/10.1016/j.micron.2008.11.004.
[28] Y. Moritz, C. Saringer, M. Tkadletz, A. Stark, N. Schell, I. Letofsky-Papst, C. Czettl, M. Pohler, N. Schalk, Oxidation behavior of arc evaporated TiSiN coatings investigated by in-situ synchrotron X-ray diffraction and HR-STEM, Surf. Coat. Technol. 404 (2020), 126632, https://doi.org/10.1016/j.surfcoat.2020.126632.
[29] M. Sperr, Z.L. Zhang, Y.P. Ivanov, P.H. Mayrhofer, M. Bartosik, Correlating elemental distribution with mechanical properties of TiN/SiNx nanocomposite coatings, Scr. Mater. 170 (2019) 20–23, https://doi.org/10.1016/j.scriptamat.2019.05.020.
[30] G. Greczynski, J. Patscheider, J. Lu, B. Alling, A. Ektarawong, J. Jensen, I. Petrov, J.E. Greene, L. Hultman, Control of Ti1-xSixN nanostructure via tunable metal-ion momentum transfer during HIPIMS/DCMS co-deposition, Surf. Coat. Technol. 280 (2015) 174–184, https://doi.org/10.1016/j.surfcoat.2015.09.001.
[31] A.O. Eriksson, O. Tengstrand, J. Lu, J. Jensen, P. Eklund, J. Rosén, I. Petrov, J. E. Greene, L. Hultman, Si incorporation in Ti1-xSixN films grown on TiN(001) and (001)-faceted TiN(111) columns, Surf. Coat. Technol. 257 (2014) 121–128, https://doi.org/10.1016/j.surfcoat.2014.05.043.
[32] L. Hultman, J. Bareño, A. Flink, H. Söderberg, K. Larsson, V. Petrova, M. Odén, J. E. Greene, I. Petrov, Interface structure in superhard TiN-SiN nanolaminates and nanocomposites: film growth experiments and ab initio calculations, Phys. Rev. B – Conden. Matter Mater. Phys. 75 (2007), https://doi.org/10.1103/PhysRevB.75.155437.
[33] B. Alling, E.I. Isaev, A. Flink, L. Hultman, I.A. Abrikosov, Metastability of fcc-related Si-N phases, Phys. Rev. B – Conden. Matter Mater. Phys. 78 (2008), https://doi.org/10.1103/PhysRevB.78.132103.
[34] M.S. Ahmed, Z.-F. Zhou, P. Munroe, L.K.Y. Li, Z. Xie, Control of the damage resistance of nanocomposite TiSiN coatings on steels: roles of residual stress, Thin Solid Films 519 (15) (2011) 5007–5012, https://doi.org/10.1016/j.tsf.2011.01.070.
[35] R. Akhter, Z. Zhou, Z. Xie, P. Munroe, Influence of substrate bias on the scratch, wear and indentation response of TiSiN nanocomposite coatings, Surf. Coat. Technol. 425 (2021) 127687, https://doi.org/10.1016/j.surfcoat.2021.127687.
[36] D. Cavaleiro, A. Cavaleiro, S. Carvalho, F. Fernandes, Oxidation behaviour of TiSiN (Ag) films deposited by high power impulse magnetron sputtering, Thin Solid Films 688 (2019) 137423, https://doi.org/10.1016/j.tsf.2019.137423.
[37] P. Xiao, B. Derby, Wetting of titanium nitride and titanium carbide by liquid metals, Acta Mater. 44 (1996) 307–314, https://doi.org/10.1016/1359-6454(95)00165-0.
[38] A.A. Mosquera, J.M. Albella, V. Navarro, D. Bhattacharyya, J.L. Endrino, Effect of silver on the phase transition and wettability of titanium oxide films, Sci. Rep. 6 (2016), https://doi.org/10.1038/srep32171.
[39] G. Greczynski, B. Bakhit, L. Hultman, M. Odén, High Si content TiSiN films with superior oxidation resistance, Surf. Coat. Technol. 398 (2020) 126087, https://doi.org/10.1016/j.surfcoat.2020.126087.
[40] J.B. Choi, K. Cho, M.-H. Lee, K.H. Kim, Effects of Si content and free Si on oxidation behavior of Ti–Si–N coating layers, Thin Solid Films 447-448 (2004) 365–370, https://doi.org/10.1016/S0040-6090(03)01083-6.
[41] A.V. Bondarev, M.N. Antonyuk, P.V. Kiryukhantsev-Korneev, T. Polcar, D.V. Shtansky, Insight into high temperature performance of magnetron sputtered Si-Ta-C-(N) coatings with an ion-implanted interlayer, Appl. Surf. Sci. 541 (2021), doi: 10.1016/j.apsusc.2020.148526.
[42] A.V. Bondarev, S. Vorotilo, I.V. Shchetinin, E.A. Levashov, D.V. Shtansky, Fabrication of Ta-Si-C targets and their utilization for deposition of low friction wear resistant nanocomposite Si-Ta-C-(N) coatings intended for wide temperature range tribological applications, Surf. Coat. Technol. 359 (2019) 342–353, https://doi.org/10.1016/j.surfcoat.2018.12.030.
[43] F. Deschaux-Beaume, T. Cutard, N. Fréty, C. Levaillant, Oxidation of a silicon nitride-titanium nitride composite: microstructural investigations and phenomenological modeling, J. Am. Ceram. Soc. 85 (7) (2002) 1860–1866, https://doi.org/10.1111/j.1151-2916.2002.tb00365.x.
[44] N. Jehanathan, Y. Liu, B. Walmsley, J. Dell, M. Saunders, Effect of oxidation on the chemical bonding structure of PECVD SiNx thin films, J. Appl. Phys. 100 (12) (2006) 123516, https://doi.org/10.1063/1.2402581.
[45] D.H. Ma, H.J. Wang, M. Niu, J.B. Wen, H. Wei, J. Zhou, J.P. Fan, D.H. Zhang, Oxidation behavior of amorphous silicon nitride nanoparticles, Ceram. Int. 44 (2018) 1443–1447, https://doi.org/10.1016/j.ceramint.2017.10.022.
[46] F. Deschaux-Beaume, T. Cutard, N. Fréty, C. Levaillant, Oxidation of a silicon nitride-titanium nitride composite: microstructural investigations and phenomenological modeling, J. Am. Ceram. Soc. 85 (2004) 1860–1866, https://doi.org/10.1111/j.1151-2916.2002.tb00365.x.
[47] Y.G. Gogotsi, F. Porz, The oxidation of particulate-reinforced Si3N4-TiN composites, Corros. Sci. 33 (1992) 627–667, https://doi.org/10.1016/0010-938X(92)90210-T.
[48] H.D. Mejía V., D. Perea, G.B. G., Development and characterization of TiAlN (Ag, Cu) nanocomposite coatings deposited by DC magnetron sputtering for tribological applications, Surf. Coat. Technol. 381 (2020) 125095, https://doi.org/10.1016/j.surfcoat.2019.125095.
[49] S. Domínguez-Meister, T.C. Rojas, J.E. Frías, J.C. Sánchez-López, Silver effect on the tribological and antibacterial properties of a-C: Ag coatings, Tribol. Int. 140 (2019) 105837, https://doi.org/10.1016/j.triboint.2019.06.030.
[50] C. Dang, J. Li, Y. Wang, J. Chen, Structure, mechanical and tribological properties of self-toughening TiSiN/Ag multilayer coatings on Ti6Al4V prepared by arc ion plating, Appl. Surf. Sci. 386 (2016) 224–233, https://doi.org/10.1016/j.apsusc.2016.06.024.
[51] F. Rose, B. Marchon, V. Rawat, D. Pocker, Q.-F. Xiao, T. Iwasaki, Ultrathin TiSiN overcoat protection layer for magnetic media, J. Vacuum Sci. Technol. A: Vacuum Surf. Films 29 (5) (2011) 051502, https://doi.org/10.1116/1.3607423.
[52] A. Al-Rjoub, L. Rebouta, N.F. Cunha, F. Fernandes, N.P. Barradas, E. Alves, W/AlSiTiNx/SiAlTiOyNx/SiAlOx multilayered solar thermal selective absorber coating, Sol. Energy 207 (2020) 192–198, https://doi.org/10.1016/j.solener.2020.06.094.
[53] Y.H. Cheng, T. Browne, B. Heckerman, P. Gannon, J.C. Jiang, E.I. Meletis, C. Bowman, V. Gorokhovsky, Influence of Si content on the structure and internal stress of the nanocomposite TiSiN coatings deposited by large area filtered arc deposition, J. Phys. D Appl. Phys. 42 (12) (2009) 125415, https://doi.org/10.1088/0022-3727/42/12/125415.
[54] A. Arranz, C. Palacio, Screening effects in the Ti 2p core level spectra of Ti-based ternary nitrides, Surf. Sci. 600 (2006) 2510–2517, https://doi.org/10.1016/j.susc.2006.04.011.
[55] N. Benito, C. Palacio, Mixed Ti-O-Si oxide films formation by oxidation of titanium-silicon interfaces, in: Applied Surface Science, Elsevier B.V, 2014, pp. 436–441, https://doi.org/10.1016/j.apsusc.2014.02.094.
[56] A. Al-Rjoub, P. Costa, L. Rebouta, M.F. Cerqueira, P. Alpuim, N.P. Barradas, E. Alves, Characterization of magnetron sputtered sub-stoichiometric CrAlSiNx and CrAlSiOyNx coatings, Surf. Coat. Technol. 328 (2017) 134–141, https://doi.org/10.1016/j.surfcoat.2017.08.038.
[57] J. Lu, T.C. Chang, Y.T. Chen, J.J. Huang, P.C. Yang, S.C. Chen, H.C. Huang, D. S. Gan, N.J. Ho, Y. Shi, A.K. Chu, Enhanced retention characteristic of NiSi2/SiNx compound nanocrystal memory, Appl. Phys. Lett. 96 (2010), https://doi.org/10.1063/1.3457870.
[58] X. Sun, H.T. Liu, H.F. Cheng, Oxidation behavior of silicon nitride fibers obtained from polycarbosilane fibers: via electron beam irradiation curing, RSC Adv. 7 (2017) 47833–47839, https://doi.org/10.1039/c7ra09056k.
[59] S.S. Rajput, S. Gangopadhyay, A. Cavaleiro, A. Al-Rjoub, C.S. Kumar, F. Fernandes, Influence of Ag additions on the structure, mechanical properties and oxidation behaviour of CrAlNAg coatings deposited by sputtering, Surf. Coat. Technol. 426 (2021) 127767, https://doi.org/10.1016/j.surfcoat.2021.127767.
[60] F. Fernandes, T.B. Yaqub, A. Cavaleiro, Influence of Ag additions on the structure, mechanical properties and oxidation behaviour of Cr-O coatings deposited by HiPIMS, Surf. Coat. Technol. 339 (2018) 167–180, https://doi.org/10.1016/j.surfcoat.2018.02.025.
[61] A. Siozios, H. Zoubos, N. Pliatsikas, D.C. Koutsogeorgis, G. Vourlias, E. Pavlidou, W. Cranton, P. Patsalas, Growth and annealing strategies to control the microstructure of AlN: AG nanocomposite films for plasmonic applications, Surf. Coat. Technol. 255 (2014) 28–36, https://doi.org/10.1016/j.surfcoat.2013.11.025.
[62] Z. Zhang, X. Zhang, Z. Xin, M. Deng, Y. Wen, Y. Song, Synthesis of monodisperse silver nanoparticles for ink-jet printed flexible electronics, Nanotechnology 22 (42) (2011), https://doi.org/10.1088/0957-4484/22/42/425601.